

**Ultrashort shock waves in nickel induced by femtosecond laser pulses**Brian J. Demaske,<sup>1</sup> Vasily V. Zhakhovsky,<sup>1</sup> Nail A. Inogamov,<sup>2</sup> and Ivan I. Oleynik<sup>1</sup><sup>1</sup>*Department of Physics, University of South Florida, Tampa, Florida 33620, USA*<sup>2</sup>*Landau Institute for Theoretical Physics, RAS, Chernogolovka 142432, Russia*

(Received 5 September 2012; revised manuscript received 23 November 2012; published 21 February 2013)

The structure and evolution of ultrashort shock waves generated by femtosecond laser pulses in single-crystal nickel films are investigated by molecular dynamics simulations. Ultrafast laser heating is isochoric, leading to pressurization of a 100-nm-thick layer below the irradiated surface. For low-intensity laser pulses, the highly pressurized subsurface layer breaks into a single elastic shock wave having a combined loading and unloading time  $\approx 10\text{--}20$  ps. Owing to the time-dependent nature of elastic-plastic transformations, an elastic response is maintained for shock amplitudes exceeding the Hugoniot elastic limit determined from simulations of steady shock waves. However, for high-intensity laser pulses (absorbed laser fluence  $>0.6$  J/cm<sup>2</sup>), both elastic and plastic shock waves are formed independently from the initial high-pressure state. Acoustic pulses emitted by the plastic front support the motion of the elastic precursor resulting in a fluence-independent elastic amplitude; whereas the unsupported plastic front undergoes significant attenuation during propagation and may fully decay within the metal film.

DOI: [10.1103/PhysRevB.87.054109](https://doi.org/10.1103/PhysRevB.87.054109)

PACS number(s): 79.20.Eb, 62.50.Ef, 02.70.Ns

**I. INTRODUCTION**

Over the years, shock compression has been established as one of the most important methods for exploring the dynamical strength of metals.<sup>1–4</sup> It is well known that a shock wave of moderate intensity consists of both elastic and plastic fronts that spatially separate in time.<sup>1–4</sup> Material passing through the elastic front is compressed uniaxially and remains in an elastic state until enough time has elapsed to transform the material into a plastic state through the generation and transport of defects. By observing how the crystal lattice evolves behind the elastic front, one may recover critical information about the processes responsible for initiating plastic deformation inside the shock wave.

The extremes of pressure and temperature generated during shock compression strongly impede real-time measurements of the sample's microstructural evolution. Therefore researchers rely on indirect observation of the dynamics at the sample's rear surface to infer major properties of the shock wave. Specifically, the velocity interferometer system for any reflector (VISAR) technique uses the Doppler shift of light to extract the velocity profile for the rear surface during reflection of the shock wave.<sup>5</sup> Rear-surface velocity profiles obtained from shock compression experiments in metals using the VISAR technique have shown, independent of impact velocity, that the amplitudes of elastic precursors were low  $\sim 0.1$  GPa and slowly decaying with propagation distance.<sup>1–4</sup> However, due to the limited time resolution of VISAR ( $>0.1$  ns), experimentalists were unable to resolve shock wave splitting in samples much less than a millimeter in thickness. New techniques based on ultrafast laser interferometry<sup>6–10</sup> and its variant, ultrafast VISAR,<sup>11–13</sup> have improved upon the time resolution of the traditional VISAR technique by several orders of magnitude. Using these improved diagnostics in recent laser-driven shock compression experiments, shock wave splitting has been resolved in micrometer and submicrometer-thick metal films.<sup>7,12,14–17</sup>

While high-velocity impactors have long been the conventional method for generating shock waves in metals,<sup>1–4</sup>

irradiation by laser pulses has recently emerged as an attractive alternative, owing to its unique ability to couple shock-wave generation and diagnostics in a single shot (pump-probe technique).<sup>7,11,12,14–18</sup> In the pioneering experimental work,<sup>7</sup> ultrashort shock waves generated by femtosecond laser pulses were investigated in submicrometer-thick Ni and Al films. In both materials, single ultrashort shock waves with amplitudes  $\approx 8$  GPa were observed. Because these amplitudes were much larger than those of the elastic precursors observed in piston-driven shock compression experiments on millimeter-thick samples, it was assumed that the ultrashort shock waves were overdriven plastic waves. Under this assumption, however, the directly measured speeds of these waves were too high. It was not until recent experiments<sup>7,12,14,15</sup> and atomistic simulations<sup>19</sup> that the source of this anomalous behavior was identified. In the case of Al, these experiments and simulations showed that ultrashort shock waves are *elastic* for pressures up to and exceeding 10 GPa.

This work investigates the response of single-crystal Ni films to loading by ultrashort shock waves generated by femtosecond laser pulses ( $<1$  ps) for a wide range of laser intensities. The first section is devoted to simulating ultrashort shock waves produced by low-intensity laser pulses under conditions similar to those in the experiments of Ref. 7. To promote direct comparison between simulated and experimental rear surface velocity profiles, the same film thicknesses are used, with the glass substrate being properly accounted for in simulation. The remaining sections deal with ultrashort shock waves produced by high-intensity laser pulses. By exploring the elastic-plastic response of Ni for shock amplitudes exceeding the Hugoniot elastic limit (HEL), these simulations provide insight into how the amplitude of the shock wave may influence the time required for plastic deformations over microscopic time and length scales.

**II. COMPUTATIONAL MODEL**

In metals, the energy of the incident laser pulse is absorbed by conduction electrons within a skin layer of

$\approx 10$  nm. Upon ultrafast internal thermalization of the electronic subsystem, the hot conduction electrons diffuse into the bulk and exchange energy with the surrounding ions.<sup>20</sup> At a time  $\tau \approx 7$  ps following laser energy absorption in Ni, the electronic and ionic subsystems have reached thermal equilibrium and the electron thermal wave has penetrated a depth  $d_T$ . For most metals including Ni, the electron-ion thermal equilibration time  $\tau$  is less than the acoustic time  $t_s = d_T/c_s$ , where  $c_s$  is the longitudinal sound speed of the irradiated material. If the thickness of the film  $l_x > d_T$ , thermal expansion of the film during laser heating is negligible; therefore a highly pressurized layer forms below the irradiated surface.<sup>21</sup>

The laser-metal interactions develop within two coupled stages. The first stage is laser energy absorption and electron-ion thermalization, which is described by a one-dimensional two-temperature hydrodynamics model (2T-HD).<sup>22</sup> The second stage includes all physical processes involving interactions among ions, and is modeled by molecular dynamics (MD). The 2T-HD and MD simulations are linked via the one-dimensional ion temperature distribution  $T_0(x)$  obtained from 2T-HD simulation at the end of the two-temperature stage,  $t = \tau \approx 7$  ps:

$$T_0(x) = T_1 e^{-x^3/d_T^3} + 300 \text{ K}, \quad (1)$$

where  $x$  is the distance from the irradiated surface,  $d_T$  is the heating depth, and  $T_1$  is related to the maximum surface temperature by  $T_s = T_1 + 300$  K. It has been shown for Au and Al that for absorbed fluences ranging between the ablation and spallation thresholds,  $d_T$  does not vary appreciably.<sup>21,23</sup> We assume the same condition holds for Ni as well. A 2T-HD simulation near the ablation threshold gives  $d_T = 60$  nm. In our simulations, we fix  $d_T$  at this value despite the fact that fluences for high-intensity laser irradiation are well beyond the spallation threshold. The laser heating is reproduced in MD simulations by establishing the  $T_0(x)$  profile through use of a Langevin thermostat that runs during the electron-ion thermalization time  $0 < t < \tau$ .

To accurately describe materials response at high temperatures and pressures induced by femtosecond laser heating, our MD simulations employ a new embedded atom method (EAM) interatomic potential for Ni. Following the approach of Ref. 23, the potential was fit to cold stress tensor components calculated by density-functional theory for a wide range of hydrostatic and uniaxial deformations as well as to experimental properties near equilibrium, such as lattice constant, cohesive energy, elastic moduli, stacking fault, vacancy formation, and vacancy migration energies. In an effort to minimize the incompatibility between the experimental and *ab initio* parts of the database, all cold stress tensor data were scaled prior to fitting. A similar rescaling of *ab initio* data was done in Ref. 24. The melting point at zero pressure simulated by the new EAM potential  $T_m = 1711$  K is in good agreement with the experimental value of 1728 K.<sup>25</sup> The simulated melting line agrees well with experimental points<sup>26–28</sup> up to pressures  $\approx 40$  GPa. The elastic and plastic branches of the Hugoniot for the new EAM potential are shown in Fig. 2. Good agreement with experiment along the plastic branch demonstrates that the new EAM potential provides a reliable description of Ni under shock

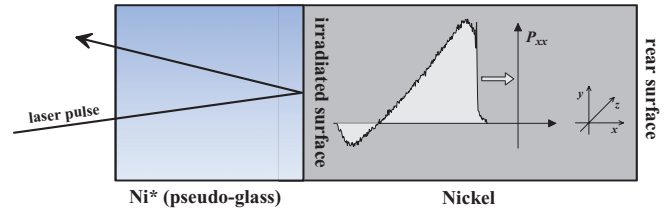


FIG. 1. (Color online) Schematic of a setup to simulate an ultrashort shock wave produced by irradiation of glass-supported nickel film by femtosecond laser pulse. For high laser intensities, a free-standing nickel film without a Ni\* pseudoglass layer is used. Profiles are spatially averaged over  $y$  and  $z$  directions.

compression. Further details regarding fitting and validation of the potential can be found in the Ref. 29.

The MD simulations are performed for samples with dimensions  $l_x \times l_y \times l_z$ , where the  $x$  axis is oriented along the direction of the laser pulse, see Fig. 1. Single-crystal samples with the  $x$  axis oriented along the [100], [110], and [111] crystallographic direction are investigated. Periodic boundary conditions are imposed along the transverse directions  $y$  and  $z$ , whereas the frontal and rear surfaces of the samples are free, see Fig. 1. All simulations presented in this paper are for samples with a transverse cross-section of  $16 \times 12$  nm<sup>2</sup>, which was found to be more than sufficient to exclude effects of transverse sample size on plasticity. In fact, samples with a much smaller transverse cross-section of  $8 \times 8$  nm<sup>2</sup> exhibit the same plastic response. The larger cross-section is used to create smoother profiles of physical variables. The thicknesses of the Ni films deposited on the glass substrate, 250, 467, and 839 nm, are the same as in experiment.<sup>7</sup>

To more closely approximate experimental samples containing many pre-existing defects, vacancies at a 0.1% concentration are randomly distributed in all samples. A major effect of the vacancies is to reduce the pressure at the HEL  $P_{\text{HEL}}$  from that of the perfect crystal.<sup>31</sup> For [110] crystal with vacancies,  $P_{\text{HEL}} = 39.6$  GPa compared to 50.6 GPa for a perfect material. The location of the HEL in Fig. 2 was obtained from piston-driven MD simulations as the onset of elastic-plastic shock-wave splitting in micrometer-thick Ni films. It was found that the pressure of the elastic precursor is not entirely pinned in the splitting regime. Rather, it is a slowly decreasing function of the piston velocity. In the case of the Ni sample with vacancies,  $P_{\text{HEL}} = 39.6$  GPa was determined at the lowest piston velocity corresponding to the onset of the plastic wave.

The glass substrate is modeled by a layer of pseudoglass composed of Ni\* pseudoatoms, see Fig. 1, which are arranged in the same crystal structure as the original Ni film. The mass of the Ni\* pseudoatoms is modified to reproduce the acoustic impedance  $Z = 11.96 \times 10^6$  kg/m<sup>2</sup>s of the glass used in experiment. The mass density of the Ni\* pseudoglass is  $\rho_{\text{Ni}^*} = Z^2/\rho_{\text{Ni}}c_s^2$ , where  $c_s$  is the longitudinal sound speed of the original Ni crystal. For samples oriented in the [110] direction,  $\rho_{\text{Ni}^*} = 0.047\rho_{\text{Ni}}$ .

In addition to the MD simulations, we continued several 2T-HD simulations past the two-temperature stage ( $t > \tau$ ) for samples with thicknesses 467 and 839 nm. The solution of the 2T-HD equations was obtained on a Lagrangian mesh; the Ni

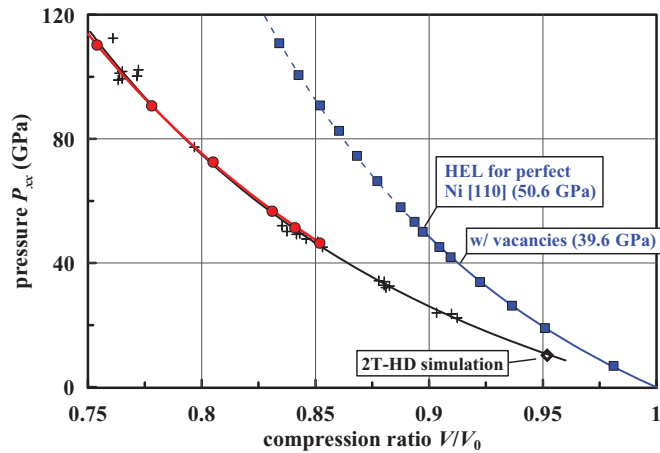


FIG. 2. (Color online) Comparison of experimental and simulated  $P$ - $V$  Hugoniot for nickel. Circles are the data points obtained from molecular dynamics (MD) simulations along the plastic branch and squares are along the elastic branch. Crosses are data from an experimental database.<sup>30</sup> The diamond is a result of a two-temperature hydrodynamics (2T-HD) simulation. The Hugoniot elastic limits (HEL) found in MD simulations of piston-driven split elastic and plastic shock waves in perfect single-crystal nickel and nickel with a 0.1% concentration of randomly distributed vacancies are shown. Dashed line indicates extension of the elastic branch to short-lived *metastable* elastic states. Note that this and all subsequent figures correspond to shock compression along the [110] direction.

crystal being considered as an isotropic plastic solid described by the wide-range multiphase equation of state.<sup>30,32</sup> Such a model for Ni provides a good description for the plastic branch of the  $P$ - $V$  Hugoniot in agreement with experiment.<sup>30</sup> The 2T-HD simulations also include the supporting pseudoglass layer.

### III. SIMULATION RESULTS

The simulation results are divided into three sections. Section (a) contains details of ultrashort shock-wave simulations performed for glass-supported Ni films irradiated by low-intensity femtosecond laser pulses under the conditions of the experiments in Ref. 7, where the intensity of the laser pulse incident on the glass was  $\sim 10^{11}$  W/cm<sup>2</sup>. Under such low-intensity irradiation, the glass remains transparent allowing the energy of the entire pulse to be transmitted to the metal surface. Therefore, in our MD simulations, the temperature profile given by Eq. (1) is applied to the Ni film *only*, such that  $x = 0$  is placed at the boundary between the pseudoglass and Ni layers of the sample (see Fig. 1).

All the data reported in this paper are obtained from the MD simulations for samples oriented along the [110] direction. Although our simulations for the two other directions ([100] and [111]) have shown similar results, the [110] direction is most relevant to the experiment of Ref. 7, where polycrystalline Ni films were used. It is expected that a weak elastic shock wave propagates in [110] single crystal Ni with a velocity close to that in a polycrystalline sample. The velocity of the weak elastic shock wave is close to the longitudinal sound speed. The theoretical longitudinal sound speeds in single-crystal Ni at normal conditions are 5.34, 5.92,

and 6.20 km/s for the [100], [110], and [111] directions, respectively, which should provide good estimates for the elastic shock-wave velocities in the corresponding directions. The experimental longitudinal sound speed in polycrystalline Ni, which provides an estimate for the elastic shock-wave velocity  $u_s$ , is 6.04 km/s.<sup>25</sup> Because the latter value is close to the theoretical sound speed along the [110] direction, we expect our single crystal [110] results to most closely match the experiment.

Sections (b) and (c) present results for MD simulations extended to higher laser intensities  $> 10^{13}$  W/cm<sup>2</sup>, which have not yet been investigated experimentally. Under such high electric field strengths, it is expected that optical breakdown of the glass occurs, thereby preventing any laser energy transmission to the metal surface.<sup>33</sup> Therefore MD simulations for the final two sections are done for free-standing Ni films, which should be used in future experiments at similar laser intensities.

#### A. Weak elastic shock waves

Heating of the film by the laser pulse is approximately isochoric over the entire electron-ion thermalization time  $t < \tau$ . This leads to a build up of pressure in a 100-nm-thick subsurface layer to the right of the pseudoglass boundary. Within this layer, the local degree of overheating  $\theta$  remains close to unity,  $\theta$  being defined as  $\theta(x) = T(x)/T_m(x)$ , where  $T_m(x)$  is the equilibrium melting temperature at position  $x$ . Because the time required for homogeneous melting for  $\theta \approx 1$  is several hundreds of picoseconds,<sup>34</sup> melting of the film proceeds slowly by heterogeneous nucleation of the liquid phase starting from the irradiated metal surface. The onset of melting is followed by decomposition of the pressure profile into two oppositely-traveling compression waves: one propagating into the pseudoglass layer, which is not considered in this work, and the another into the bulk of the Ni film. The thickness of the pseudoglass layer was sufficient to exclude the return of the wave reflected at the left boundary of the sample (shown in Fig. 1) during the time interval relevant to the experiment.<sup>7</sup>

The amplitudes  $P_{xx}^{\max}$  of the shock waves observed in experiment for all sample thicknesses were  $\approx 8$  GPa.<sup>7</sup> To generate a compression wave in the Ni film of the same amplitude requires an absorbed fluence  $F_{\text{abs}} \approx 50$  mJ/cm<sup>2</sup> in our MD simulations. Due to an increase in the sound speed  $c_s$  with compression, the wave front steepens as it travels through the film. This process of wave-breaking continues until a thin shock front spanning a few lattice planes has formed. The complete process of wave breaking is illustrated in Fig. 3 for an 839-nm film. For 250 and 467-nm films, the wave front is still steepening upon reaching the rear surface. For these cases, the wave incident at the rear surface of the film is not a shock, but rather a sharp compression wave. Material entering the shock (sharp compression) wave is brought to a state along the elastic branch of the  $P$ - $V$  Hugoniot, see Fig. 2, then unloaded through the release tail without undergoing any plastic deformation. Therefore, the waves observed in our MD simulations are *elastic*, which is consistent with the fact that their amplitudes ( $\approx 8$  GPa) are much less than the theoretical  $P_{\text{HEL}}$ , see Fig. 2. In an attempt to induce plasticity at lower pressures, a grain

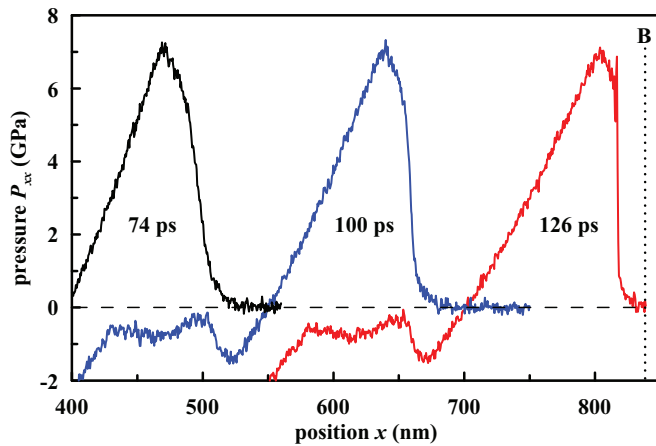


FIG. 3. (Color online) Several snapshots of a single elastic ultrashort shock wave propagating in an 839-nm nickel film obtained from molecular dynamics simulations. Rear surface of the sample shown in Fig. 1 is marked by the vertical dotted line B.

boundary is inserted along the  $x$  axis. However, even in such cases, the shock wave remains elastic.

The rear surface displacement profiles of the Ni film upon reflection of the shock wave for both experiment and MD simulations are shown in Fig. 4 for two different thicknesses of film. The elastic shock waves simulated by MD arrive 4.6 and 4 ps earlier than the shock waves observed in experiment for 467 and 839-nm films, respectively. Also shown is the rear surface displacement profile from a 2T-HD simulation of a plastic shock wave in an 839-nm Ni film. The difference in arrival time for the plastic shock wave simulated by 2T-HD and experiment is  $\approx 28$  ps, whereas there is no significant difference in the shock amplitude. Such a discrepancy provides evidence that the shock waves observed in experiment were not overdriven plastic waves.

The acoustic approximation  $u_p = u_f/2$  is used in shock compression experiments to obtain the particle velocity  $u_p$

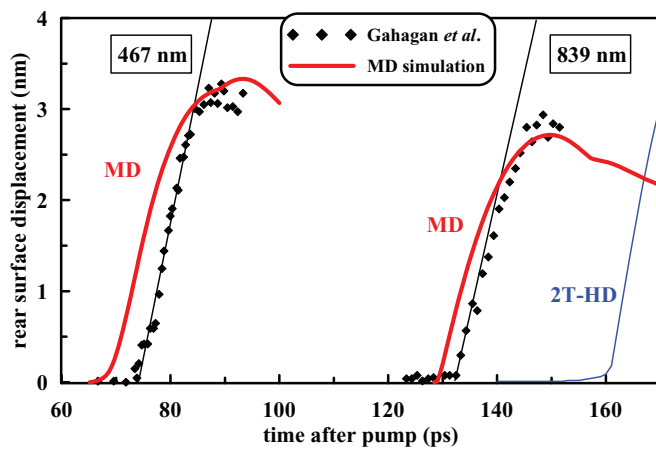


FIG. 4. (Color online) Rear-surface displacement profiles upon arrival of the ultrashort shock wave. Solid curves are molecular dynamics (MD) (thick curves) and hydrodynamics (HD) (thin curve) simulations. Diamonds are transformed phase shift data obtained from experiment.<sup>7</sup> Solid lines are linear fits to the experimental points used in this work to determine maximum rear-surface velocity  $u_f^{\max}$ .

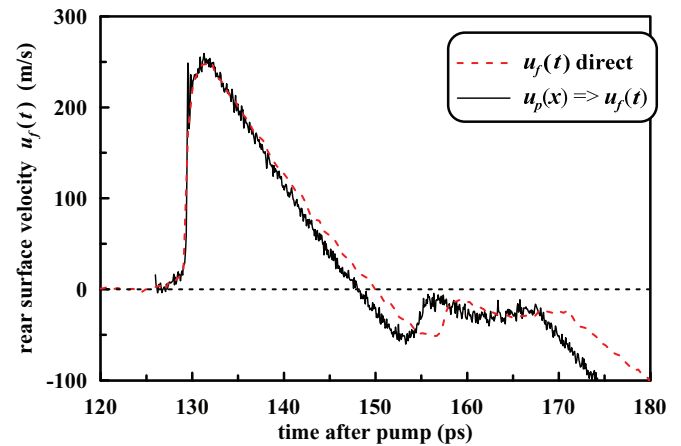


FIG. 5. (Color online) Check of acoustic approximation: rear-surface velocity profiles from the molecular dynamics simulation of a single elastic ultrashort shock wave. Solid curve is the transformed spatial velocity profile at the moment when the shock wave arrives at the rear surface, while dashed (red) curve is obtained directly from the simulation.

from the rear-surface velocity  $u_f$  upon reflection of the shock wave. As a check on the accuracy of this approximation, the inverse transformation  $u_f(t) = 2u_p(x/c_s)$  is applied to the simulated one-dimensional spatial profile of the particle velocity  $u_p(x)$  of the shock wave arriving at the rear surface at  $x = 0$ . The transformed  $u_p(x) \Rightarrow u_f(t)$  history for the MD simulation of an 839-nm film is shown in Fig. 5 alongside the rear-surface velocity profile obtained directly from simulation. Good agreement between these two profiles confirms that the acoustic approximation is valid for ultrashort shock waves having similar amplitudes.

In experiment, the shock velocity  $u_s$  was determined via two methods: indirect - from a measurement of the maximum value of  $u_p$ , the corresponding  $u_s$  being read from the appropriate branch of the  $u_p$ - $u_s$  Hugoniot; and direct - from the measured shock propagation time and the known thickness of the film. It is clear that the indirect method gives an instantaneous value for  $u_s$  taken at the moment when the shock arrives at the rear surface, whereas the direct method yields an average velocity. For the indirect method, a linear fit to the rear-surface displacement data is first used to determine the maximum rear-surface velocity  $u_f^{\max}$ , see Fig. 4. Then, using the acoustic approximation, the maximum value of  $u_p = u_f^{\max}/2$ . For the case of the 839-nm film, the maximum values of  $u_p$  obtained from experiment and MD simulation are 132 and 130 m/s, respectively. Using the experimental plastic branch of the  $u_p$ - $u_s$  Hugoniot  $u_s = 4.60 + 1.437u_p$ ,<sup>7</sup> the relevant plastic shock velocity is  $u_s = 4.79$  km/s, which is well below the direct experimental measurement of  $6.15 \pm 0.39$  km/s. Similar disagreement between the experimental values for  $u_s$  determined using the direct and indirect methods is also found for the 250- and 467-nm films.

A way to resolve the contradiction between the two seemingly comparable methods for determining  $u_s$  is suggested by our MD simulations: the shock waves observed in experiment are *elastic* despite having an amplitude an order of magnitude greater than those observed in piston-driven

shock compression experiments on millimeter-thick samples. Therefore the *elastic* branch of the  $u_p$ - $u_s$  Hugoniot must be used in place of the plastic branch to determine  $u_s$  via the indirect method. Using the calculated elastic branch of the  $u_p$ - $u_s$  Hugoniot for the [110] direction  $u_s = 5.92 + 1.976u_p$ , the relevant *elastic* shock velocity is  $u_s = 6.18$  km/s for the 839-nm film, which lies within the uncertainty provided by the direct experimental measurement of  $6.15 \pm 0.39$  km/s. Likewise, the *corrected* shock velocities for the 250 and 467-nm films also agree well with direct experimental measurements.

One might ask whether these two methods (indirect and direct) yield substantially different values for  $u_s$  due to attenuation of the shock wave during the course of propagation. As an illustration of the degree of attenuation observed in our MD simulations, a compression wave beginning to propagate near the irradiated surface with a velocity of 6.28 km/s reaches the rear surface of the 839-nm film with a slightly smaller velocity of 6.20 km/s. The relatively weak attenuation ( $\approx 1.2 \times 10^{-4}$  km/s per nanometer) cannot explain the much larger discrepancy between the two experimental values for  $u_s$  obtained using the indirect and direct methods. Therefore we conclude that the shock waves observed in Ref. 7 were single *elastic* waves despite their exceptionally high peak pressure of  $\approx 8$  GPa.

### B. Strong elastic shock waves

To determine the threshold for the splitting of an ultrashort shock wave into an elastic precursor and plastic wave, simulations at laser fluences higher than those presented in the previous section are necessary to induce an initial pressurization greater than  $P_{\text{HEL}}$ . In contrast to the low-intensity laser irradiation explored in the previous section, where heating can be considered isochoric during the full heating time  $\tau$ , heating by high-intensity pulses is approximately isochoric only within the first few picoseconds after laser energy absorption  $t_{\text{iso}} < \tau$ . For times  $t > t_{\text{iso}}$ , the highly-pressurized subsurface layer relaxes, leading to the formation of compression and rarefaction waves that alter the local density  $\rho$  of the film.

At the beginning of laser heating ( $t < t_{\text{iso}}$ ), the degree of overheating near the irradiated Ni surface is relatively large,  $\theta(x) \gtrsim 1.2$ , and melting proceeds rapidly by homogeneous nucleation of liquid droplets inside the overheated solid. Because the target temperature profile  $T_0(x)$  decays quickly inside the sample, as seen in Eq. (1), the heating rate is highest at the irradiated surface and decreases towards the bulk. The lifetime of the overheated solid is a decreasing function of  $\theta$ .<sup>34</sup> Therefore material near the surface, where  $\theta(x)$  is large, melts more quickly than material lying farther away. The differences in melting times along the thickness of the sample results in the apparent supersonic motion of the melting front. It is worth noting that the melting front is not a wave because its motion is a direct result of the nonuniform heating rate applied to the film. The movement of the melting front into cooler regions is associated with a reduction in  $\theta(x)$ . Both the density  $\rho$  and degree of overheating  $\theta$  uniquely specify the thermodynamic state within a specific region of the sample. Because the density of the film  $\rho$  remains close to the initial density  $\rho_0 = 8.9$  g/cc at any time prior to  $t_{\text{iso}}$ , we conclude that the pressure and temperature of material near the melting front at  $t = t_{\text{iso}}$ , where

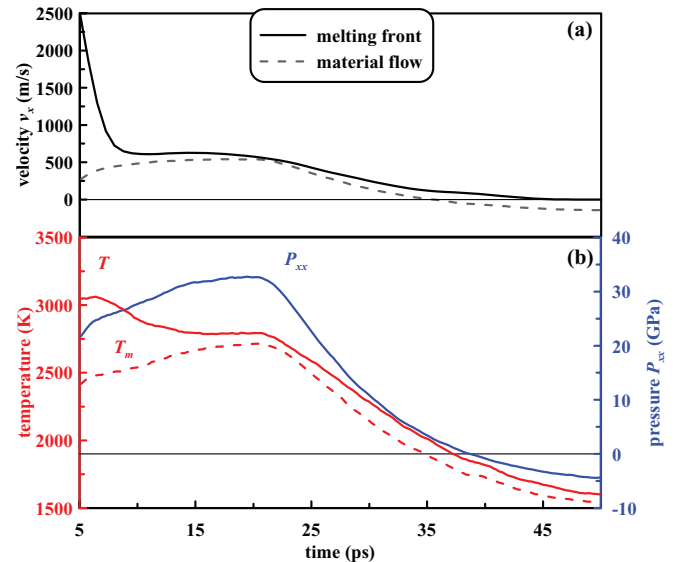


FIG. 6. (Color online) Thermodynamical and flow parameters at the melting front at  $t > t_{\text{iso}}$  for an absorbed fluence of  $0.32$  J/cm<sup>2</sup>. (a) Solid line shows the velocity of the melting front with respect to the static reference frame of the simulation box, while dashed line shows the instantaneous material flow velocity. (b) Progression of the temperature  $T$ , local equilibrium melting temperature  $T_m$ , and normal component of pressure  $P_{xx}$ .

$\theta \approx 1.25$ , must be independent of  $F_{\text{abs}}$ , whereas the width of the molten zone increases with deposited energy. In general, the thermodynamic properties at the melting front are uniquely determined by the melting line and the degree of overheating. Therefore, melting transitions follow a single trajectory on both  $P$ - $T$  and  $\rho$ - $T$  phase diagrams irrespective of laser fluence (see Sec. III C for details).

For times  $t > t_{\text{iso}}$ , shear stresses become nonzero within the sample signaling the end of isochoric heating and the beginning of adiabatic heating associated with the propagation of the compression wave out of the liquid metal subsurface layer to the solid bulk of the film. Within several picoseconds after  $t_{\text{iso}}$ , the dominant melting mechanism shifts from homogeneous nucleation to normal heterogeneous nucleation. The shift is associated with an appreciable deceleration of the melting front to subsonic velocities; see Fig. 6(a). Continued propagation of the compression wave into the solid causes the pressure at the melting front to rise, further reducing  $\theta$  until it reaches its minimum value near unity [see temperature at  $t = 23$  ps in Fig. 6(b)]. At the point of maximum compression, the melting front has slowed to  $\approx 30$  m/s in the local coordinate system moving with material flow velocity. Adiabatic expansion associated with the rarefaction wave leads to an increase in  $\theta$  near the melting front, which then begins to accelerate slowly in the reference frame of the moving material until reaching a nearly constant speed of  $\sim 100$  m/s between 35 and 50 ps; see Fig. 6(a). Not shown in the figure, after  $t = 50$  ps the melting front begins to decelerate, eventually stopping at 55 ps, and then reversing its motion during recrystallization.

Although the pressure at the melting front at  $t = t_{\text{iso}}$  is independent of  $F_{\text{abs}}$ , the maximum pressure, which is attained inside the molten layer, increases with  $F_{\text{abs}}$ . Thus, the amplitude of the compression wave emitted into the bulk

of the sample, which corresponds to roughly half of this maximum pressure, is strongly dependent on absorbed fluence. As an example, consider a simulation for  $F_{\text{abs}} = 0.32 \text{ J/cm}^2$ . At  $t = t_{\text{iso}}$  the maximum pressure within the molten zone is in excess of 50 GPa, whereas at the melting front the pressure is significantly lower,  $\approx 20 \text{ GPa}$ . Upon emission of the compression wave into the solid, the pressure at the melting front increases and reaches its maximum of  $\approx 33 \text{ GPa}$  before rapidly decaying due to the coming rarefaction wave. As the amplitude of the compression wave is still below  $P_{\text{HEL}}$ , no plasticity develops within the sample, and a single elastic shock wave is formed. As in the case of the weak elastic shock wave described in the previous section, the time required for wave breaking is considerable, and a shock front does not form until the compression wave has propagated a distance of  $\approx 600 \text{ nm}$ .

The purely elastic response continues up to a threshold absorbed fluence  $F_{\text{th}} \approx 0.6 \text{ J/cm}^2$ , at which point a small amount of plastic deformation is observed at the edge of the melting front where the barrier for dislocation nucleation is lower than in the bulk. However, away from the melting front, a strong *elastic* shock wave develops with an amplitude  $P_{xx}^{\text{max}} \approx 48 \text{ GPa} > P_{\text{HEL}}$ . The absence of a secondary plastic front can be attributed to the extremely short duration of shock compression, where the lifetime of a material particle passing through the ultrashort shock wave is  $\approx 20 \text{ ps}$ . Because no new dislocations can be generated during this time, the material remains in a *metastable* elastic state passing through the shock wave virtually unchanged. All such states that can be reached by shock compression lie on a continuation of the elastic branch of the Hugoniot above the HEL (see Fig. 2). As in the case of a weak elastic shock wave, the rarefaction tail causes the shock wave to attenuate during propagation. Immediately after the shock front forms, its velocity is  $u_s = 7.81 \text{ km/s}$ . Upon reaching the rear side of the sample,  $u_s$  drops to a final value of  $7.58 \text{ km/s}$ . During that time, the shock wave travels a distance of  $400 \text{ nm}$ . Assuming a constant attenuation rate, it would decay completely after propagating  $\approx 7 \mu\text{m}$ .

### C. Split elastic and plastic shock waves

For absorbed fluences  $> 0.6 \text{ J/cm}^2$ , the compression wave transmitted into the solid from the initial highly-pressurized liquid subsurface layer breaks into elastic and plastic shock waves. The  $P$ - $T$  progression at the melting front for several values of  $F_{\text{abs}}$  above the threshold for plastic wave formation is shown in Fig. 7. Isochoric heating for times  $t < t_{\text{iso}}$  results in the same, almost vertical trajectory in the  $\rho$ - $T$  phase diagram for all considered fluences; see inset in Fig. 7. It is evident from the  $P$ - $T$  diagram that after isochoric heating the temperature at the melting front decreases slowly with time, while pressure rises due to passage of the compression wave. Although there is adiabatic heating of the material near the melting front as a result of the compression, the effect is strongly counteracted by propagation of the melting front into cooler parts of the sample.

The large increase in the melting temperature due to the increasing pressure results in a rapid deceleration of the melting front as shown by the dashed to solid line transition in the trajectory M of the melting front in Fig. 8(b). The liquid and solid regions of the sample are differentiated using the

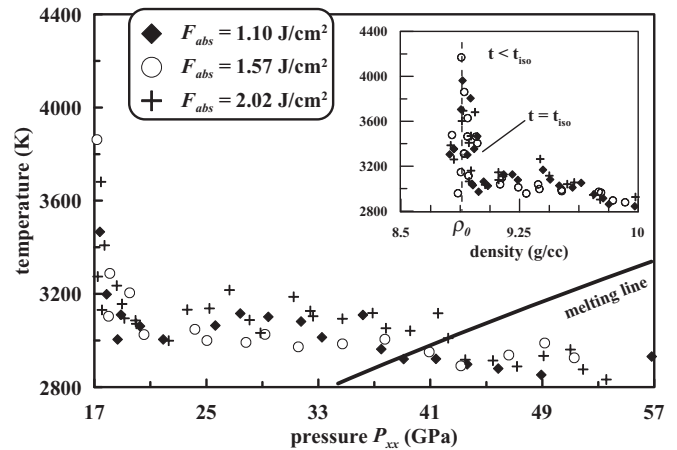


FIG. 7. Fluence-independent  $P$ - $T$  progression of material at the melting front for three absorbed fluences above the threshold for the formation of split elastic and plastic shock waves. Solid curve is the simulated equilibrium melting line for Ni. Inset shows the same progression in  $\rho$ - $T$  space, where the initial density of the film is  $\rho_0 = 8.9 \text{ g/cc}$ . Time increases from left to right.

local order parameter<sup>35</sup>  $Q_6$  averaged over the cross-section of the sample. This parameter has already been successfully used in analysis of MD simulations of shock wave propagation in metals to determine solid-liquid transitions.<sup>36,37</sup> At the melting front,  $Q_6$  drops below the critical value of 0.407, which corresponds to the transition from solid to liquid phase. At the moment when the  $P$ - $T$  trajectory of the melting front in Fig. 7 intersects with the melting line, the flow velocity is  $0.8 \text{ km/s}$ , and the density of the solid at the interface is  $9.9 \text{ g/cc}$  (compared to the initial  $\rho_0 = 8.9 \text{ g/cc}$ ) for all considered fluences. Further compression leads to supercooling of the liquid ( $\theta < 1$ ) as the equilibrium melting temperature rises (due to the increase in pressure) above the local temperature at the melting front.

From Fig. 7, it is evident that for all three values of  $F_{\text{abs}} > 0.6 \text{ J/cm}^2$ , the density, pressure, and temperature at the melting front progress in a similar manner. Based on these results, we conclude that the thermodynamics at the melting front is fluence independent. As the compression wave continues to pass through the melting front, the shear stresses within the solid increase. At the moment when the shear stress  $\tau = \frac{1}{2}[P_{xx} - \frac{1}{2}(P_{yy} + P_{zz})]$  reaches the critical value of  $\approx 17.8 \text{ GPa}$ , the emission of dislocations starts from the surface of the liquid-solid interface. Continued propagation of the compression wave into the solid results in the multiplication and further production of dislocations, which eventually form the plastic shock front (see Fig. 9). The leading part of the compression wave emitted into the bulk of the sample prior to the onset of plasticity has an amplitude of  $\approx 50 \text{ GPa}$ . Because the pressure at the melting front is independent of fluence, so too are the shear stresses within the solid just ahead of it. Therefore the elastic shock wave, which forms out of the leading part of the compression wave that passes through the melting front, will have an amplitude of  $\approx 50 \text{ GPa}$  independent of absorbed fluence, provided that the amplitude of the compression wave is greater than the fluence threshold for shock splitting  $F_{\text{th}} \approx 0.6 \text{ J/cm}^2$ . In contrast,

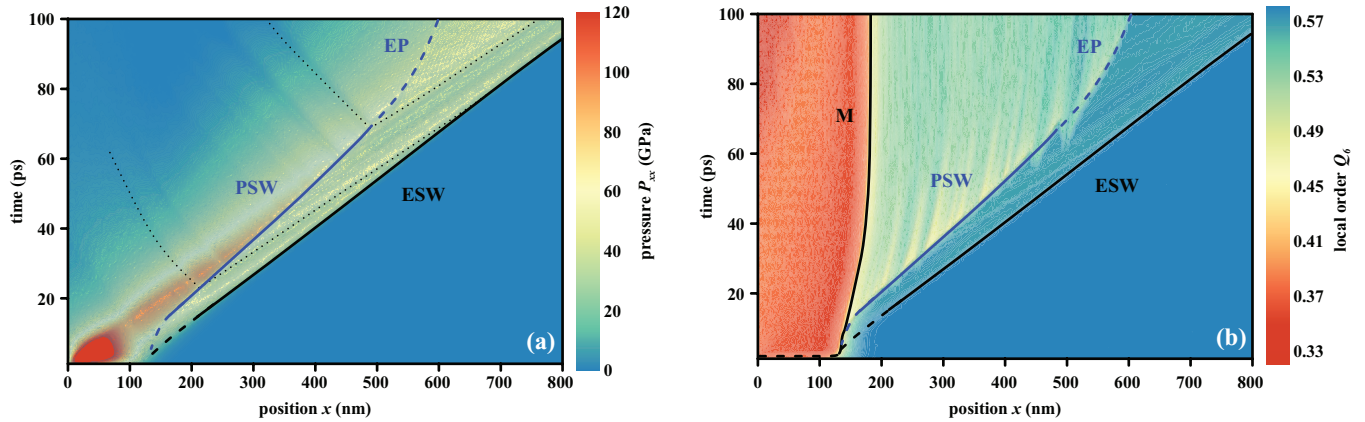


FIG. 8. (Color online)  $x$ - $t$  contour maps of (a) pressure  $P_{xx}$  and (b) local-atomic-order parameter<sup>35</sup>  $Q_6$  for an MD simulation at an absorbed laser fluence of  $1.57 \text{ J/cm}^2$ . The trajectories of the elastic (ESW) and plastic (PSW) shock wave fronts are shown in both (a) and (b), while the melting front (M) is shown in (b) only. Pairs of acoustic waves are generated as a result of elastic-plastic transformation events that occur within the plastic front. The trajectories of two pairs of acoustic waves (out of many) are shown by the dotted lines in (a) originating from the PSW trajectory. After dropping below 55 GPa, the plastic front decays, while the elastic-plastic transition layer (EP) continues to propagate through the film as a subsonic front.

below this threshold, the amplitude of the elastic shock wave is strongly dependent on the absorbed fluence, as was discussed in the previous section.

The two independent processes of elastic and plastic wave breaking of the laser-induced compression wave are shown in Fig. 9 for a simulation at an absorbed fluence of  $1.57 \text{ J/cm}^2$ . Elastic and plastic wave breaking occur nearly simultaneously at  $t = 14 \text{ ps}$ , though at distinct positions within the film, see Fig. 9. The leading elastic shock front (ESW) forms at the position  $x = 200 \text{ nm}$ , and has an amplitude  $P_{xx} = 30 \text{ GPa}$ . The plastic shock front (PSW) forms within the transition

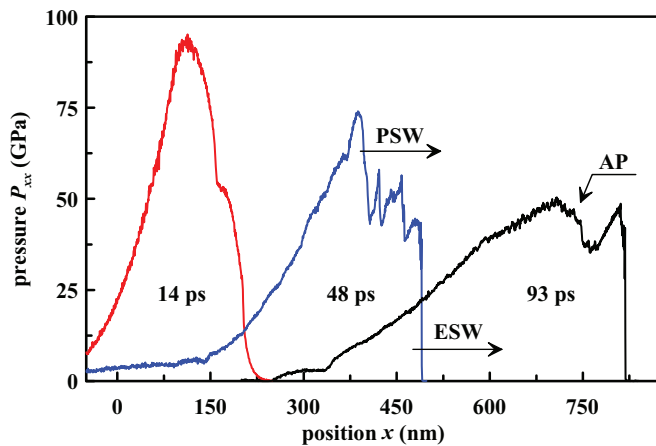


FIG. 9. (Color online) Snapshots showing the development of the ultrashort shock wave from an MD simulation at an absorbed laser fluence of  $1.57 \text{ J/cm}^2$ . The initial compression wave breaks into a leading elastic shock wave (ESW) followed by a slower moving plastic shock wave (PSW) at  $t = 14 \text{ ps}$ . The plastic front emits several triangle-shaped acoustic pulses moving within the elastically compressed material between ESW and PSW (see the profile at  $t = 48 \text{ ps}$ ). By 93 ps, the PSW has decayed completely after emitting a final acoustic pulse. Their trajectories within the sample are shown in Fig. 8.

layer separating the elastic and plastically deformed regions of material located at  $x = 160 \text{ nm}$ , where  $P_{xx} = 64 \text{ GPa}$ . The trajectories of ESW and PSW are shown in Fig. 8. Material behind the plastic front is more disordered than either uncompressed or elastically-compressed material and can be identified by a reduction in the average local order parameter  $Q_6$ —the same parameter that is used to distinguish solid and liquid phases. In fact,  $Q_6$  is sensitive enough to distinguish between uncompressed and elastically compressed materials. While  $Q_6 = 0.5636$  is in uncompressed solid, in the elastically compressed material it is reduced to the range  $0.54 \leq Q_6 \leq 0.56$ , and in plastically deformed material it is further reduced to the range  $0.45 \leq Q_6 \leq 0.522$ . The color contrast between uncompressed, elastically compressed, plastic, and liquid regions of the sample can be seen clearly in Fig. 8(b).

Material passing through the elastic front is compressed to a point along the *metastable* extension of the elastic branch of the Hugoniot (see Fig. 2). Upon nearing the plastic front, the incoming elastic material is compressed even further, approaching the final pressure at the peak of the plastic shock wave. The gradient of pressure within this thin layer of overcompressed elastic material produces a compression wave that, because of its high speed, begins to separate from the plastic front. However, the overcompressed elastic material is highly unstable and, within a few picoseconds, dislocations nucleate, start to grow, and multiply. This elastic-plastic collapse is accompanied by a sudden release of shear stress and a drop in pressure, which in turn produces two oppositely-traveling rarefaction waves: one propagating within the plastically deformed material, and the other coupling to the remaining part of the overcompressed elastic wave, together forming a single triangle-shaped acoustic pulse that travels towards the leading elastic shock front.

The processes of overcompression of elastic material and elastic-plastic decay near the plastic front occur repeatedly as the shock wave propagates through the sample, thereby producing several backward-moving rarefaction and

forward-moving acoustic pulses. A few acoustic pulses can be clearly seen in Fig. 9 within the profile corresponding to  $t = 48$  ps. The trajectories of the first and last pairs of rarefaction and acoustic pulses are shown as dotted lines in Fig. 8(a). Such pairs of pulses originate at the point of elastic-plastic collapse, and then separate as the rarefaction pulse travels down the rarefaction tail of the ultrashort shock wave and the acoustic pulse travels towards the leading elastic front. Given enough time, the forward-moving acoustic pulses eventually merge with the leading elastic front, as shown by the right dotted line merging with the ESW trajectory; see Fig. 8(a). The formation of acoustic pulses is not a specific feature of ultrashort shock waves as it has already been observed in MD simulations of steady two-zone elastic-plastic shock waves.<sup>31</sup>

Initially, the plastic front has a velocity almost equal to that of the elastic front, which is evident by the equal slopes of ESW and PSW in Fig. 8. However, due to a lack of supporting pressure, the plastic front attenuates in time. The process of attenuation is ongoing until  $\approx 70$  ps when the plastic front decays completely. Its disappearance coincides with its amplitude dropping below 55 GPa, whereupon it emits a final acoustic pulse (AP), see Fig. 9. It is clear from the figure that AP has a higher amplitude than the leading elastic front and, given enough time, would reach it. The subsonic leftover from the decay of the plastic shock wave is not itself a wave, but instead is the separating layer between elastic and plastic regions of the film. Further propagation of this elastic-plastic transition layer (EP) can be attributed to the growth and multiplication of existing dislocations at the edge of the plastic zone, where material remains under shear stress produced by the leading elastic wave. Due to the relatively small thickness of the films used in our MD simulations, the motion of EP for times  $> 120$  ps is complicated by reflection of the elastic shock wave from the rear surface. Nevertheless, EP finally stops due to relaxation of the shear stresses within the sample. The final position of EP within the sample is dependent on the time needed for the decay of the plastic shock wave, which in turn depends on the initial amplitude of the laser-induced compression wave. It follows that higher absorbed fluences will result in deeper penetration of plastic deformation inside the film.

#### IV. DISCUSSION

The results of MD simulations of ultrashort shock waves in Ni films combined with the analysis of the experiments in Ref. 7 performed in this work unambiguously demonstrate that the shock waves observed in these experiments were *elastic* despite amplitudes far exceeding the conventional value for the HEL of  $\sim 0.1$  GPa measured in experiments of split shock waves in millimeter-thick samples or larger. This conclusion has been reached based on the following facts: (a) shock velocities  $u_s$  directly measured in experiment are in good agreement with those obtained indirectly using knowledge of the piston velocity  $u_p$  and *elastic* branch of the Hugoniot; (b) shock-wave attenuation is a minor effect and cannot account for the large discrepancy between direct measurements of  $u_s$  and indirect determination of  $u_s$  using the *plastic* branch of the  $u_p$ - $u_s$  Hugoniot, as was done in Ref. 7; and (c) if it were an overdriven plastic shock wave of similar amplitude,

then it would arrive at the rear surface much later relative to both MD simulations and experiment, as was shown by 2T-HD simulations.

The high elastic amplitudes of the ultrashort shock waves observed in Ni extend the already well-established picture of time-dependent elastic-plastic transformations<sup>38,39</sup> to the picosecond time scale. Under such fast loading conditions, the relaxation process in our simulated single-crystal Ni samples, within which there are no pre-existing dislocation sources, is homogeneous dislocation nucleation. The critical shear stress for this process is  $\tau_{cr} \simeq G/10$ ,<sup>40</sup> where  $G$  is the shear modulus. Because  $\tau_{cr}$  is much larger than the critical shear stress required for the multiplication of pre-existing dislocations, the dislocation-free material is able to withstand substantial deformations without plasticity. To obtain an estimate of the characteristic time for homogeneous dislocation nucleation  $\tau_p$  in Ni under conditions similar to the ultrashort shock waves observed in our MD simulations, an ensemble of NVE reference systems is used to represent the uniaxially compressed material behind the elastic front.<sup>41</sup> As for shocked material, the vacancy concentration of 0.1% was present in the reference systems. Taking  $P_{xx} = 50.6$  GPa, shear stress  $\tau = 17.7$  GPa, and temperature  $T = 425$  K, as input parameters for one set of reference system calculations,  $\tau_p \approx 10$  ps; whereas at  $P_{xx} = 50.0$  GPa,  $\tau = 17.3$  GPa, and at  $T = 425$  K,  $\tau_p \approx 30$  ps. Simulations within the split wave regime confirm the latter value of  $P_{xx}$ , as they display homogeneous dislocation nucleation at shock pressures greater than 50 GPa and no dislocation nucleation at smaller shock wave intensities. Because the total loading-unloading time  $t_c = 10$ – $20$  ps for the ultrashort shock waves in our MD simulations matches the characteristic time of homogeneous dislocation nucleation, it becomes clear why there is the sudden onset of plasticity at such high shock intensities.

#### V. CONCLUSIONS

By directly comparing our shock-wave velocities and rear-surface displacement profiles obtained from our MD and 2T-HD simulations to those obtained in experiment,<sup>7</sup> we showed that ultrashort shock waves generated by low-intensity femtosecond laser pulses in Ni films propagate as elastic waves with pressure exceeding, by an order of magnitude, the pressure within the elastic precursors observed in piston-driven and nanosecond laser shock compression experiments.<sup>1–4</sup> The same high-pressure elastic behavior has also been found in micrometer-thick Al films in recent laser-based shock compression experiments<sup>12,14,15,17</sup> and MD simulations.<sup>19</sup>

Furthermore, our MD simulations show a purely elastic response for absorbed fluences up to the threshold fluence of  $0.6$  J/cm<sup>2</sup>, beyond which the ultrashort shock wave splits into elastic and plastic components. Because the shock wave generated by a femtosecond laser pulse is unsupported, the plastic front attenuates with propagation distance. Once the amplitude of the plastic front drops below the critical pressure of 50 GPa, it decays into an elastic wave, leaving behind a sample in which only a partial region is plastically deformed. We suggest the use of this property of ultrashort shock waves in future laser-driven shock compression experiments

to manually control the depth of plastic deformations inside an irradiated metal sample by changing the intensity of the incident laser pulse.

#### ACKNOWLEDGMENTS

This work is supported by the National Science Foundation under Grant No. DMR-1008676 and Defense Threat

Reduction Agency under Grant No. HDTRA1-12-1-0023. B.J.D. is supported by the Department of Defense (DoD) through the National Defense Science & Engineering Graduate Fellowship (NDSEG) Program. N.A.I. is supported by the Russian Foundation for Basic Research. Calculations were performed using NSF XSEDE facilities, the USF Research Computing Cluster, and computational facilities of the Materials Simulation Laboratory at USF Physics Department.

- <sup>1</sup>G. I. Kanel, S. V. Razorenov, and V. E. Fortov, *Shock-Wave Phenomena and the Properties of Condensed Matter* (Springer, New York, 2004).
- <sup>2</sup>Y. B. Zel'dovich and Y. P. Raizer, *Physics of Shock Waves and High-Temperature Hydrodynamic Phenomena* (Dover, New York, 2002).
- <sup>3</sup>R. A. Graham, *Solids Under High-Pressure Shock Compression: Mechanics, Physics, and Chemistry* (Springer, Berlin, 1993).
- <sup>4</sup>G. E. Duvall, in *Physics of High Energy Density*, edited by P. Caldirola and H. Knoepfel (Academic Press, New York, 1971).
- <sup>5</sup>L. M. Barker and R. E. Hollenbach, *J. Appl. Phys.* **43**, 4669 (1972).
- <sup>6</sup>D. J. Funk, D. S. Moore, K. T. Gahagan, S. J. Buelow, J. H. Reho, G. L. Fisher, and R. L. Rabie, *Phys. Rev. B* **64**, 115114 (2001).
- <sup>7</sup>K. T. Gahagan, D. S. Moore, D. J. Funk, R. L. Rabie, S. J. Buelow, and J. W. Nicholson, *Phys. Rev. Lett.* **85**, 3205 (2000).
- <sup>8</sup>K. T. Gahagan, D. S. Moore, D. J. Funk, J. H. Reho, and R. L. Rabie, *J. Appl. Phys.* **92**, 3679 (2002).
- <sup>9</sup>C. A. Bolme, S. D. McGrane, D. S. Moore, and D. J. Funk, *J. Appl. Phys.* **102**, 033513 (2007).
- <sup>10</sup>S. D. McGrane, D. S. Moore, D. J. Funk, and R. L. Rabie, *Appl. Phys. Lett.* **80**, 3919 (2002).
- <sup>11</sup>M. R. Armstrong, J. C. Crowhurst, S. Bastea, and J. M. Zaug, *J. Appl. Phys.* **108**, 023511 (2010).
- <sup>12</sup>J. C. Crowhurst, M. R. Armstrong, K. B. Knight, J. M. Zaug, and E. M. Behymer, *Phys. Rev. Lett.* **107**, 144302 (2011).
- <sup>13</sup>M. R. Armstrong, J. C. Crowhurst, S. Bastea, W. M. Howard, J. M. Zaug, and A. F. Goncharov, *Appl. Phys. Lett.* **101**, 101904 (2012).
- <sup>14</sup>S. I. Ashitkov, M. B. Agranat, G. I. Kanel', P. S. Komarov, and V. E. Fortov, *JETP Lett.* **92**, 516 (2010).
- <sup>15</sup>V. H. Whitley, S. D. McGrane, D. E. Eakins, C. A. Bolme, D. S. Moore, and J. F. Bingert, *J. Appl. Phys.* **109**, 013505 (2011).
- <sup>16</sup>J. M. Winey, B. M. LaLone, P. B. Trivedi, and Y. M. Gupta, *J. Appl. Phys.* **106**, 073508 (2009).
- <sup>17</sup>L. Huang, Y. Yang, Y. Wang, Z. Zheng, and W. Su, *J. Phys. D* **42**, 045502 (2009).
- <sup>18</sup>A. Loveridge-Smith, A. Allen, J. Belak, T. Boehly, A. Hauer, B. Holian, D. Kalantar, G. Kyrala, R. W. Lee, P. Lomdahl *et al.*, *Phys. Rev. Lett.* **86**, 2349 (2001).
- <sup>19</sup>V. V. Zhakhovskii and N. A. Inogamov, *JETP Lett.* **92**, 521 (2010).
- <sup>20</sup>S. I. Anisimov and B. Luk'yanchuk, *Physics-Uspeschi* **45**, 293 (2002).
- <sup>21</sup>B. J. Demaske, V. V. Zhakhovskiy, N. A. Inogamov, and I. I. Oleynik, *Phys. Rev. B* **82**, 064113 (2010).
- <sup>22</sup>S. Anisimov, B. Kapelovich, and T. Perel'man, *Zh. Eksp. Teor. Fiz.* **66**, 776 (1974).
- <sup>23</sup>V. V. Zhakhovskii, N. A. Inogamov, Y. V. Petrov, S. I. Ashitkov, and K. Nishihara, *Appl. Surf. Sci.* **255**, 9592 (2009).
- <sup>24</sup>Y. Mishin, D. Farkas, M. J. Mehl, and D. A. Papaconstantopoulos, *Phys. Rev. B* **59**, 3393 (1999).
- <sup>25</sup>D. R. Lide and T. J. Bruno, in *CRC Handbook of Chemistry and Physics, 93rd edition*, edited by W. M. Haynes, D. R. Lide, and T. J. Bruno (CRC Press, Boca Raton, FL, 2012).
- <sup>26</sup>D. Errandonea, B. Schwager, R. Ditz, R. Boehler, and M. Ross, *Phys. Rev. B* **63**, 132104 (2001).
- <sup>27</sup>S. Japel, B. Schwager, R. Boehler, and M. Ross, *Phys. Rev. Lett.* **95**, 167801 (2005).
- <sup>28</sup>P. Lazor, G. Shen, and S. K. Saxena, *Phys. Chem. Miner.* **20**, 86 (1993).
- <sup>29</sup>B. J. Demaske, V. V. Zhakhovskiy, C. T. White, and I. I. Oleynik, *AIP Conf. Proc.* **1426**, 1211 (2012).
- <sup>30</sup>Shock wave database: <http://teos.ficp.ac.ru/rusbank/>.
- <sup>31</sup>V. V. Zhakhovskiy, M. M. Budzevich, N. A. Inogamov, I. I. Oleynik, and C. T. White, *Phys. Rev. Lett.* **107**, 135502 (2011).
- <sup>32</sup>A. V. Bushman, G. I. Kanel', A. L. Ni, and V. E. Fortov, *Intense Dynamic Loading of Condensed Matter* (Taylor and Francis, London, 1993).
- <sup>33</sup>D. von der Linde and H. Schüler, *J. Opt. Soc. Am. B* **13**, 216 (1996).
- <sup>34</sup>B. Rethfeld, K. Sokolowski-Tinten, D. von der Linde, and S. Anisimov, *Phys. Rev. B* **65**, 092103 (2002).
- <sup>35</sup>P. J. Steinhardt, D. R. Nelson, and M. Ronchetti, *Phys. Rev. B* **28**, 784 (1983).
- <sup>36</sup>V. I. Levitas and R. Ravelo, *Proceedings of the National Academy of Sciences* **109**, 13204 (2012).
- <sup>37</sup>M. M. Budzevich, V. V. Zhakhovskiy, C. T. White, and I. I. Oleynik, *Phys. Rev. Lett.* **109**, 125505 (2012).
- <sup>38</sup>J. W. Taylor, *J. Appl. Phys.* **36**, 3146 (1965).
- <sup>39</sup>Y. M. Gupta, *J. Appl. Phys.* **46**, 3395 (1975).
- <sup>40</sup>D. Hull and D. J. Bacon, *Introduction to Dislocations* (Butterworth-Heinemann, Oxford, UK, 2001).
- <sup>41</sup>The reference system consists of a sample of Ni crystal having the same orientation and dimensions as the elastic zone within an elastic-plastic ultrashort shock wave. The atomic positions of the initially room-temperature sample are then scaled along the shock direction such that the scaled system has the same mass density as the material immediately behind the elastic front. After scaling, the system is heated by a thermostat for  $\approx 1$  ps and then monitored until a homogeneous dislocation nucleation event occurs.